ACS NANO

www.acsnano.org

ARTICLE

Ti_3C_2 MXene-Derived Sodium/Potassium Titanate Nanoribbons for High-Performance Sodium/Potassium Ion Batteries with Enhanced Capacities

Yanfeng Dong,[†] Zhong-Shuai Wu,[*,†] Shuanghao Zheng,[†,§,⊥] Xiaohui Wang,[‡] Jieqiong Qin,[†,⊥] Sen Wang,[†,⊥] Xiaoyu Shi,[†,§,∥] and Xinhe Bao[†,§]

[†]Dalian National Laboratory for Clean Energy and [§]State Key Laboratory of Catalysis, Dalian Institute of Chemical Physics, Chinese Academy of Sciences, 457 Zhongshan Road, Dalian 116023, People's Republic of China

[‡]Shenyang National Laboratory for Materials Science, Institute of Metal Research, Chinese Academy of Sciences, 72 Wenhua Road, Shenyang 110016, People's Republic of China

[⊥]University of Chinese Academy of Sciences, 19 A Yuquan Road, Shijingshan District, Beijing 100049, People's Republic of China

[∥]Department of Chemical Physics, University of Science and Technology of China, 96 JinZhai Road, Hefei 230026, People's Republic of China

Supporting Information

ABSTRACT: Sodium and potassium ion batteries hold promise for next-generation energy storage systems due to their rich abundance and low cost, but are facing great challenges in optimum electrode materials for actual applications. Here, ultrathin nanoribbons of sodium titanate (M-NTO, $NaTi_{1.5}O_{8.3}$) and potassium titanate (M-KTO, $K_2Ti_4O_9$) were successfully synthesized by a simultaneous oxidation and alkalization process of Ti_3C_2 MXene. Benefiting from the suitable interlayer spacing (0.90 nm for M-NTO, 0.93 nm for M-KTO), ultrathin thickness (<11 nm), narrow widths of nanoribbons (<60 nm), and open macroporous structures for enhanced ion insertion/extraction kinetics, the resulting M-NTO exhibited a large reversible capacity of 191 mAh g^{-1} at 200 mA g^{-1} for sodium storage, higher than those of pristine Ti_3C_2 (178 mAh g^{-1}) and commercial TiC derivatives (86 mAh g^{-1}). Notably, M-KTO displayed a superior reversible capacity of 151 mAh g^{-1} at 50 mA g^{-1} and 88 mAh g^{-1} at a high rate of 300 mA g^{-1} and long-term stable cyclability over 900 times, which outperforms other Ti-based layered materials reported to date. Moreover, this strategy is facile and highly flexible and can be extended for preparing a large number of MXene-derived materials, from the 60+ group of MAX phases, for various applications such as supercapacitors, batteries, and electrocatalysts.

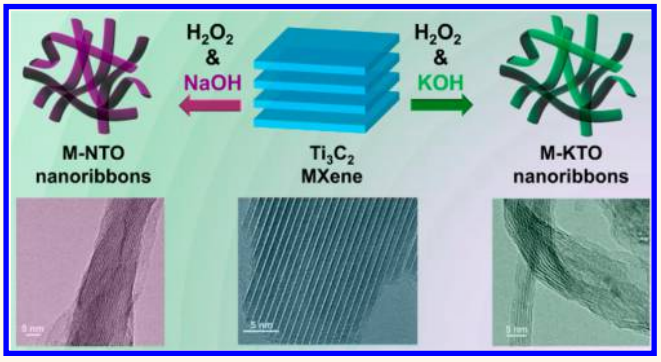

KEYWORDS: *MXene, sodium titanate, potassium titanate, nanoribbons, sodium ion batteries, potassium ion batteries*

Lithium ion batteries (LIBs) are being widely used in portable electronic devices and large-scale grid storage applications, which however could be greatly hampered by never-ceasing concerns of limited lithium resources, rising cost, and safety issues.[1−3] To address this issue, sodium ion batteries (SIBs) and potassium ion batteries (PIBs) are promising as ideal alternatives to LIBs for energy storage applications due to their rich abundance (Na, K), low cost, high theoretical capacities, and similar redox potentials ($E_{Na^+/Na}$ = −2.7 V, $E_{K^+/K}$ = −2.9 V) to lithium ($E_{Li^+/Li}$ = −3.0 V).[2,4−9] Unfortunately, larger ionic radii of Na^+ (1.02 Å) and K^+ (1.38 Å) in comparison with Li^+ (0.76 Å) result in totally different electrochemical behaviors of SIBs and PIBs from LIBs.[10,11] For example, graphite is the most well-known anode for LIBs and also exhibits a reversible capacity of 207 mAh g^{-1} for PIBs,[9] but shows poor record for Na storage in most electrolytes.[12] Furthermore, the huge volume expansion and sluggish kinetics in most electrodes (*e.g.*, metal oxide, porous carbon) induced

Received: February 19, 2017
Accepted: May 1, 2017
Published: May 1, 2017

DOI: 10.1021/acsnano.7b01165
ACS Nano 2017, 11, 4792−4800

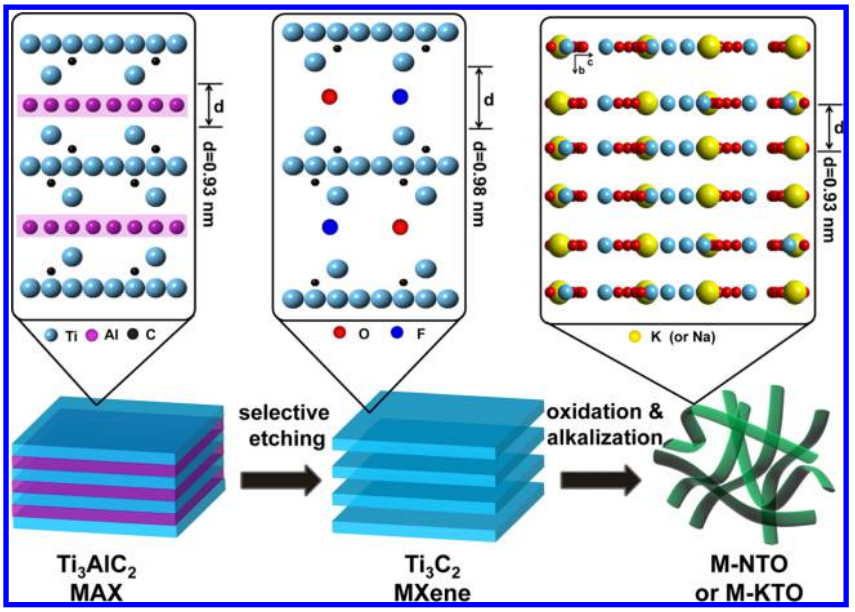

Figure 1. Schematic of the fabrication of M-NTO or M-KTO nanoribbons. First, Ti_3C_2 MXene was fabricated *via* selectively etching Al of Ti_3AlC_2 MAX phase in 40% HF. Second, Ti_3C_2 MXene was hydrothermally treated with NaOH or KOH solution in the presence of H_2O_2 at 140 °C for 12 h, producing M-NTO or M-KTO nanoribbons.

by large Na^+ or K^+ ions usually lead to low capacities and/or fast capacity fading.[11,13] Therefore, urgent development of nanostructural electrode materials with enhanced charge storage mechanism is highly required to meet the coming era of next-generation batteries (SIBs, PIBs).

Ti-based layered materials, such as sodium/potassium titanate and Ti-based MXene (*e.g.*, Ti_3C_2, Ti_2C), have been intensively explored in SIBs and PIBs due to their suitable interlayer spacing for accommodating Na^+/K^+ ions, low working potentials, exceptional chemical durability, and environmental benignity.[4,14−17] Note that electrochemical performances of these materials are strongly dependent on their nanostructures. For instance, $Na_2Ti_3O_7$ nanotubes exhibited high reversible capacities of 245 mAh g^{-1} at 50 mA g^{-1} and 155 mAh g^{-1} at 2 A g^{-1},[14] while microspherical $Na_2Ti_3O_7$ delivered only a low capacity of 108 mAh g^{-1} at 350 mA g^{-1}.[18] Furthermore, potassium titanates ($K_2Ti_4O_9$ and $K_2Ti_8O_{17}$) were also evaluated for PIBs, however their uncontrollable nanostructures offered low capacities (<100 mAh g^{-1} at 50 mA g^{-1}) and limited cycling life (<100 times).[19,20] Moreover, two-dimensional (2D) MXene nanosheets (*e.g.*, Ti_3C_2) have gained enormous attention because of their high conductivity,[21−24] flexible interlayer space,[25−27] tailored surface chemistry[28,29] and promising applications in LIBs, SIBs, and PIBs with a theoretical capacity of 447.8, 351.8, and 191.8 mAh g^{-1}, respectively.[30,31] However, these HF-etched multilayer MXene nanosheets, terminated by oxygen- and fluorine-containing groups, usually show severe structural defects, leading to large initial irreversible capacities and limited reversible capacities of 164 mAh g^{-1} for SIBs and 146 mAh g^{-1} for PIBs.[2,32] Therefore, designing well-defined layered Ti-based nanostructures with suitable interlayer spacing and stable structure, using innovative synthesis strategies, is of great significance for improving sodium and potassium storage kinetics of SIBs and PIBs. Very recently, layered TiO_2@ $Ti_3C_2T_x$ heterogeneous structures for enhanced lithium storage were reported by one-step oxidation transformation of MXene ($Ti_3C_2T_x$), which greatly inspired us to develop a class of MXene-derived materials with well-defined structures for energy storage.[33] To the best of our knowledge, there is no report on MXene-derived Ti-based layered materials for SIBs and PIBs so far.

Here we report the transformation of accordion-like Ti_3C_2 MXene into ultrathin nanoribbons of sodium titanate (M-NTO, $NaTi_{1.5}O_{8.3}$) and potassium titanate (M-KTO, $K_2Ti_4O_9$) as high-performance anode materials for SIBs and PIBs, respectively. Ultrathin layered M-NTO and M-KTO nanoribbons were fabricated by selective etching of the Ti_3AlC_2 MAX phase, followed by simultaneous oxidation and alkalization processes of HF-etched Ti_3C_2 nanosheets. Both the ion insertion/extraction kinetics and structural stability were greatly improved by the resulting nanostructures of M-NTO and M-KTO, such as the suitable interlayer spacing (0.90 nm for M-NTO, 0.93 nm for M-KTO), ultrathin thickness (<11 nm), narrow widths of nanoribbons (<60 nm), and open macroporosity; therefore, the resulting M-NTO exhibited an enhanced reversible capacity of 191 mAh g^{-1} at 200 mA g^{-1} for SIBs, higher than those of pristine Ti_3C_2 (178 mAh g^{-1}) and commercial TiC derivative (86 mAh g^{-1}). Furthermore, M-KTO offered superior potassium storage, such as a high reversible capacity of 151 mAh g^{-1} at 50 mA g^{-1}, high rate capacity of 88 mAh g^{-1} at 300 mA g^{-1}, and long cycling life over 900 times, outperforming the Ti-based anodes for PIBs reported to date.

RESULTS AND DISCUSSION

A schematic for synthesizing MXene (Ti_3C_2)-derived titanate nanoribbons of M-NTO ($NaTi_{1.5}O_{8.3}$) or M-KTO ($K_2Ti_4O_9$) was illustrated in Figure 1. First, the pristine Ti_3AlC_2 MAX phase was prepared by solid−liquid reaction of ball-milled Ti, Al, and graphite powder in a molar ratio of 3:1.1:1.88 at 1550 °C for 2 h under an argon flow.[34] Second, Ti_3C_2 MXene nanosheets were synthesized by selectively etching the Al layer from the pristine Ti_3AlC_2 phase with HF acid (Figure S1).[35,36] Third, M-NTO or M-KTO nanoribbons were fabricated *via* simultaneous oxidation and alkalization of Ti_3C_2 MXene in a

DOI: 10.1021/acsnano.7b01165
ACS Nano 2017, 11, 4792−4800

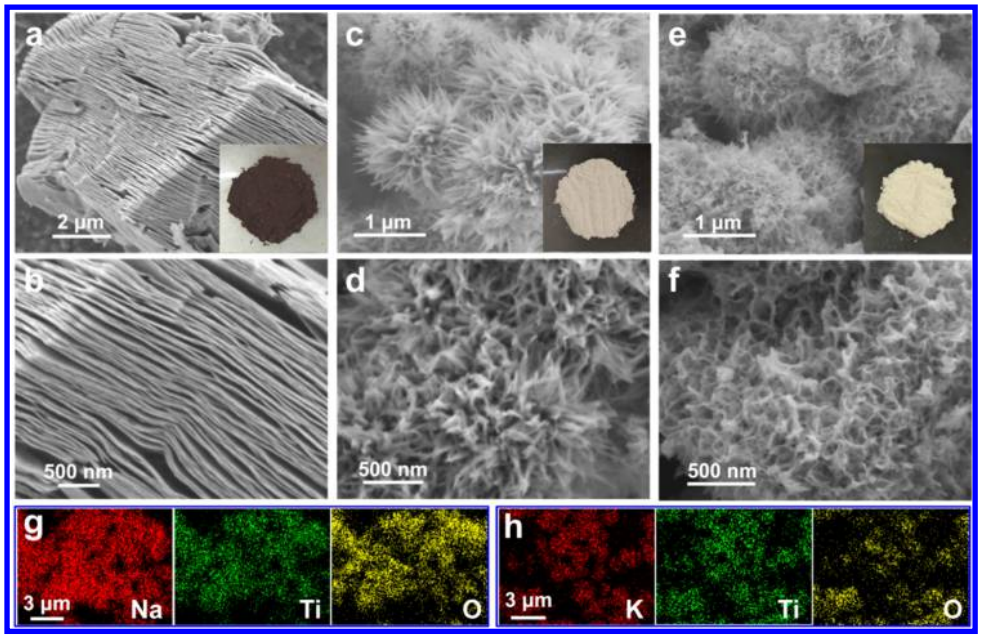

Figure 2. SEM images of (a and b) Ti_3C_2 MXene, (c and d) M-NTO, and (e and f) M-KTO. The insets in (a), (c), and (e) are photographs of Ti_3C_2 MXene, M-NTO, and M-KTO powder, respectively. (g, h) Elemental mapping analysis of (g) M-NTO and (h) M-KTO.

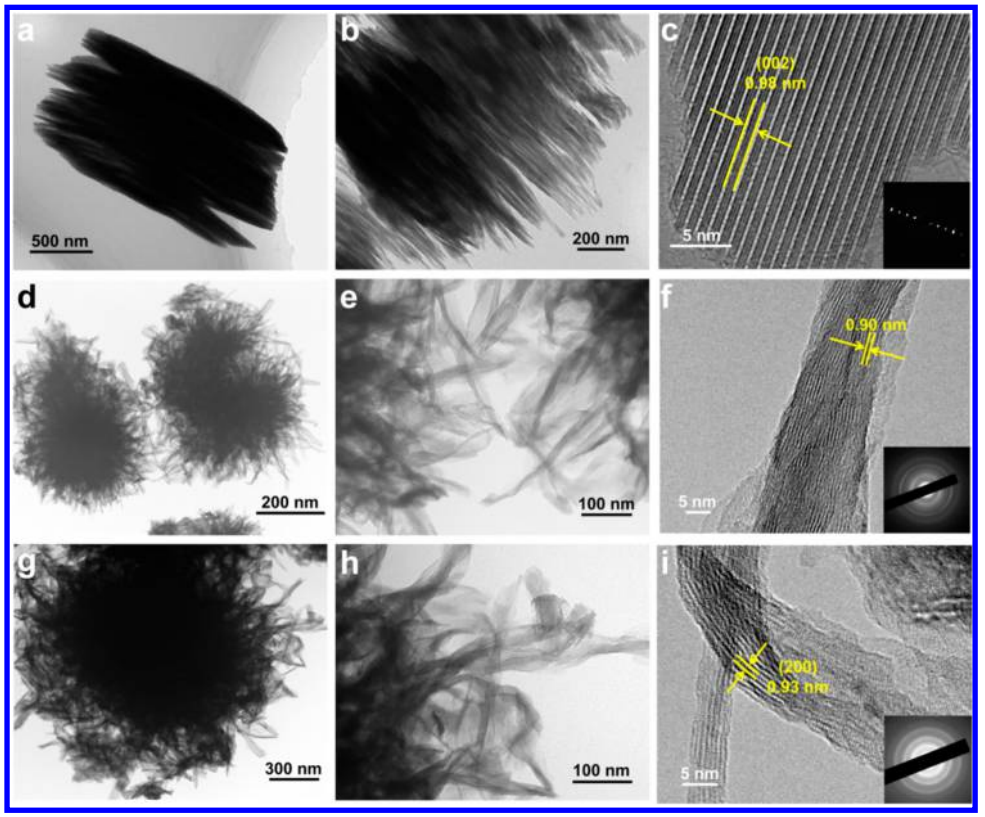

Figure 3. (a, b) TEM and (c) HRTEM images of Ti_3C_2 MXene. (c, d) TEM and (f) HRTEM images of M-NTO. (g, h) TEM and (i) HRTEM images of M-KTO. The insets in (c), (f), and (i) are the corresponding SAED patterns.

mixed solution of 1 M alkaline solution (NaOH or KOH) and 30% H_2O_2 at 140 °C for 12 h. Importantly, this strategy is simple and avoids high temperature.

Scanning electron microscopy (SEM) of Ti_3C_2 MXene is shown in Figure 2a and b. A panoramic view revealed an accordion-like multilayer nanostructure, indicative of the successful fabrication from densely packed Ti_3AlC_2 (Figure 1, Figure S1).[36−38] A high-magnification SEM image disclosed the thickness of the exfoliated multilayers ranging from 30 to 50 nm (Figure 2b). After hydrothermal treatment of Ti_3C_2 MXene in NaOH and H_2O_2 solution, the color changed from black-red (Figure 2a) to white (Figure 2c), suggestive of the transformation of MXene into M-NTO. The SEM image displayed urchin-like morphology of M-NTO, and a high-magnification

DOI: 10.1021/acsnano.7b01165
ACS Nano 2017, 11, 4792−4800

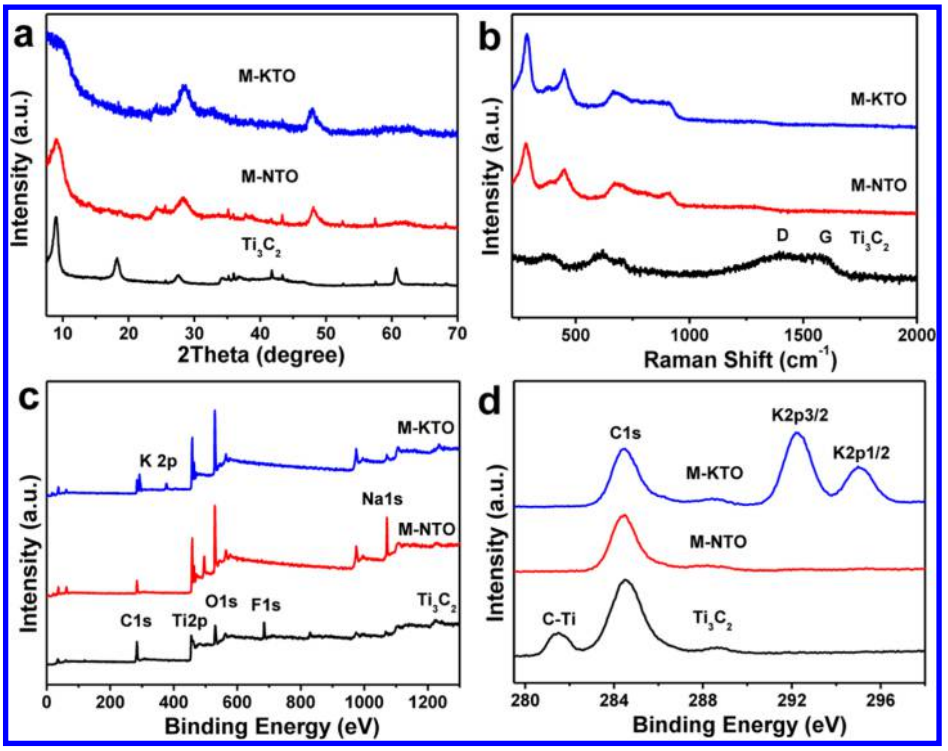

Figure 4. (a) XRD patterns, (b) Raman spectra, and (c) XPS full spectra of Ti_3C_2 MXene, M-NTO, and M-KTO. (d) C1 XPS spectra of Ti_3C_2 and M-NTO, and C 1s and K 2p XPS spectrum of M-KTO.

SEM image further evidenced the curved structures of M-NTO nanoribbons (Figure 2d). While Ti_3C_2 MXene was treated in a KOH and H_2O_2 system, a light yellow product of M-KTO was obtained and showed a self-woven framework with open macroporosity (Figure 2e and f), which was different from the relatively straight nanoribbons of M-NTO. Furthermore, elemental mapping visualized the homogeneous element distribution of Na, Ti, and O in M-NTO (Figure 2g) and K, Ti, and O in M-KTO (Figure 2h), respectively.

Transmission electron microscopy (TEM) and high-resolution TEM (HRTEM) images further revealed the structural evolution from Ti_3C_2 MXene nanosheets to M-NTO and M-KTO nanoribbons. As shown in Figure 3a–c, Ti_3C_2 MXene exhibited microscale bulk particles with multilayer structures, and HRTEM manifested multilayered crystalline structure, with a typical interlayer spacing of ~0.98 nm, which was also confirmed by the dotted-line pattern in selected area electron diffraction (SAED). Interestingly, after a simultaneous oxidation and alkalization process, nanosphere-like aggregates with a diameter of <1 μm were found, consisting of randomly elongated nanoribbons (Figure 3e). Notably, TEM and HRTEM images validated the narrow widths of 15–50 nm and ultrathin thickness of 4–11 nm of M-NTO nanorribons (Figure S2). The width or thickness is much smaller than those of pristine Ti_3C_2 MXene and reported titanate nanoribbons or nanosheets,[33,39–41] demonstrating the advantages of the transformation strategy in nanostructural design. M-NTO also showed the layered nanostructures with an interlayer spacing of 0.90 nm and multiring pattern in SAED (Figure 3f). The M-KTO aggregate was slightly larger than that of M-NTO, but still smaller than that of Ti_3C_2 bulk particles (Figure 3g). M-KTO nanoribbons presented highly curved and intertwined structures (Figure 3h), with widths of 28–60 nm and thicknesses of 3.5–11 nm (Figure S3). Moreover, a large interlayer spacing of 0.93 nm, corresponding to the (200) plane of M-KTO, was identified in Figure 3i.

X-ray diffraction (XRD) patterns, Raman spectra, and X-ray photoelectron spectroscopy (XPS) were also recorded of the phase transformation. As shown in Figure 4a, a strong peak at 9.0° was assigned to in-plane diffraction (002) of Ti_3C_2 with a *d*-spacing of ~0.98 nm, well consistent with the reported literature.[35] After the oxidation and alkalization process, the typical diffraction peaks at 18° and 60° of Ti_3C_2 disappeared, and new peaks at 24.3° and 48° were observed in both M-NTO and M-KTO. Furthermore, a strong peak at ~9.3° for M-NTO and at ~9.2° for M-KTO was recognized. The chemical composition of M-KTO was analyzed as $K_2Ti_4O_9$ (JCPDS 32-0861),[20] and M-NTO was evaluated as $NaTi_{1.5}O_{8.3}$ based on XRD and elemental analysis of Na:Ti:O (Figures S4 and S5). Raman spectra confirmed the disappearance of a broad C peak of Ti_3C_2 MXene ranging from 1300 to 1600 cm^{-1}, and accordingly, two strong peaks were observed at ~280 and ~450 cm^{-1} for both M-NTO and M-KTO (Figure 4b).[17,42] Moreover, XPS spectra disclosed a remarkable F 1s signal and C–Ti signal of Ti_3C_2 MXene at 686 and 281.5 eV, but both of them are not observable in the case of M-NTO and M-KTO (Figure 4c and d). Notably, the Na 1s signal at 1074 eV and K 2p signals (K $2p_{3/2}$ at ~292 eV and K $2p_{1/2}$ at ~295 eV) were well affirmed in the full XPS spectrum of M-NTO and K 2p-C 1s spectrum of M-KTO (Figure 4c and d), respectively.

On the basis of the above observation, we proposed a possible mechanism for the formation of Ti_3C_2 MXene-derived ultrathin M-NTO or M-KTO nanoribbons as follows. First, Ti_3C_2 was oxidized to TiO_2, as confirmed by XRD and SEM characterizations (Figures S6a and S7).[43] Second, the alkalization process of TiO_2 under hydrothermal conditions promoted the formation of sodium or potassium titanates.[44] It should be mentioned that the alkalized Ti_3C_2 without involving

DOI: 10.1021/acsnano.7b01165
ACS Nano 2017, 11, 4792–4800

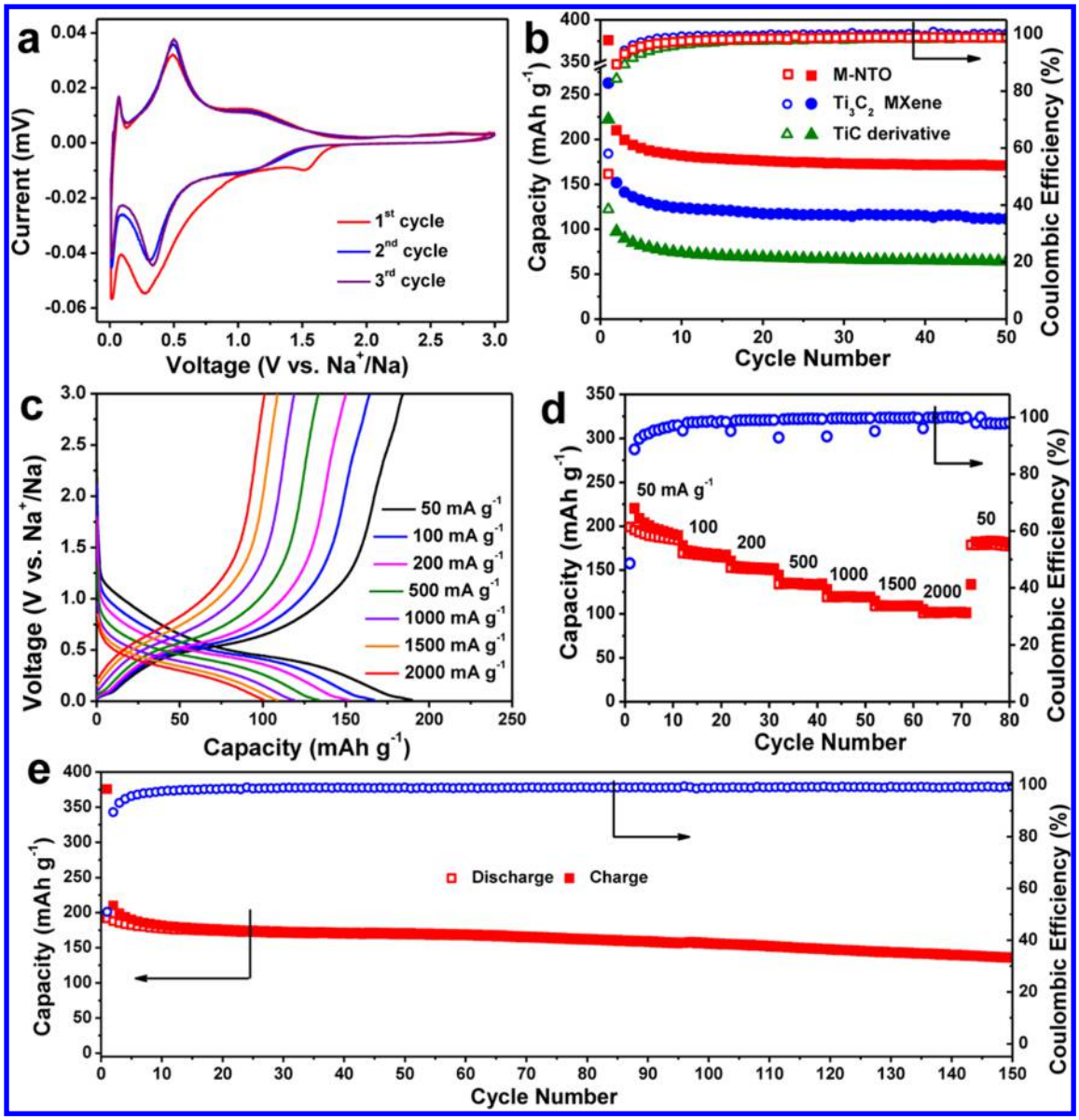

Figure 5. Electrochemical characterization of M-NTO for SIBs in 1 M $NaCF_3SO_3$ electrolyte. (a) Cyclic voltammetry of M-NTO measured at 0.1 mV s^{-1}. (b) Cycling stability and Coulombic efficiencies of M-NTO, Ti_3C_2 MXene, and commercial TiC derivative at a current density of 200 mA g^{-1}. (c) Galvanostatic charge and discharge curves of M-NTO cycled at different current densities from 50 to 2000 mA g^{-1}. (d) Rate performance of M-NTO at different current densities. (e) Long-term cycling performance and Coulombic efficiency of M-NTO for SIBs at 200 mA g^{-1}.

H_2O_2 treatment still maintained layered structures of MXene and cannot achieve nanoribbion-like structures of M-NTO and M-KTO (Figure S6b). Furthermore, during the alkalization process in a suitable concentration (Figure S8), the small titanate nanosheets appeared at an early stage (~2 h) on the surface of bulk MXene particles (Figure S6c). With the progress of alkalization, longer curved nanoribbons were formed, then assembling into urchin-like spheres in M-NTO or intertwined frameworks in M-KTO. Third, MXene as a highly active Ti precursor is the key for the synthesis of M-NTO or M-KTO nanoribbons. For comparison, commercial TiC particles were also hydrothermally treated by the similar procedure of M-NTO, and the final products were denoted as commercial TiC derivative. However, neither the nanorbbion structure or phase transformation was obtained (Figures S6d–f and S7). Noteworthy, our simultaneous oxidation and alkalization process operated at low temperature, and the alkaline solution is highly flexible for preparing MXene-derived titanate nanoribbons, which has never been achieved by traditional alkali hydrothermal treatment of TiO_2 precursors (Table S1).

The suitable interlayer spacing (0.9 nm for M-NTO, 0.93 nm for M-KTO), ultrathin thickness (<11 nm), narrow widths (<60 nm), and open macroporous structures of nanoribbons, such M-NTO and M-KTO are highly favorable for high-performance sodium and potassium storage.[45,46] To this end, electrochemical properties of M-NTO and M-KTO were evaluated as anodes for SIBs and PIBs, respectively. Figure 5a showed cyclic voltammetry (CV) curves of M-NTO for the first three cycles, measured between 0.01 and 3.0 V (*vs* Na^+/Na) at 0.1 mV s^{-1} in 1 M $NaCF_3SO_3$ electrolyte. In the first discharge cycle, two main cathodic peaks were observed at 1.53 and 0.25

DOI: 10.1021/acsnano.7b01165
ACS Nano 2017, 11, 4792–4800

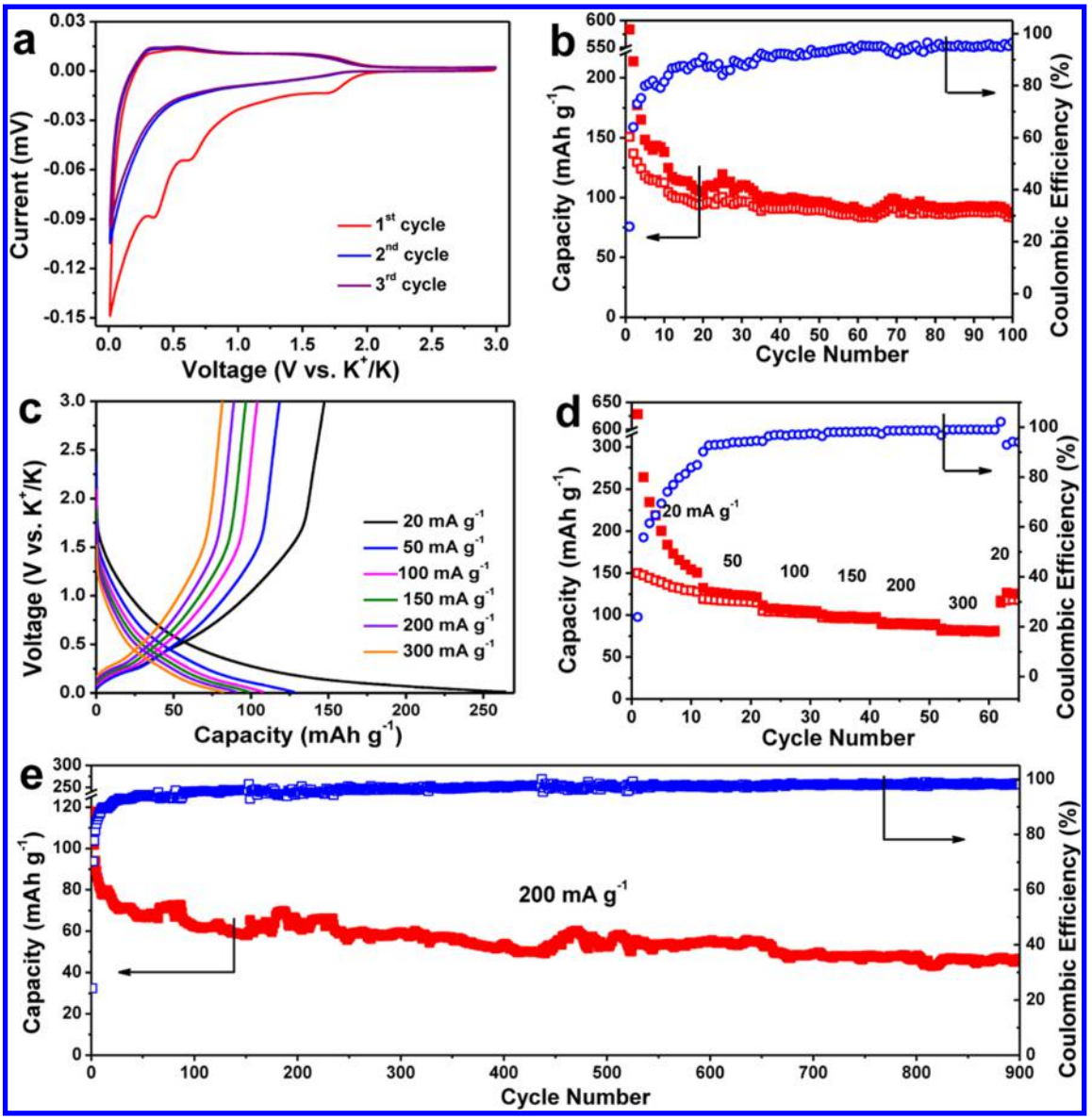

Figure 6. Electrochemical characterization of M-KTO for PIBs in 1.0 M KPF_6 electrolyte. (a) Cyclic voltammetry of M-KTO measured at 0.1 mV s^{-1}. (b) Cycling stability of M-KTO at 50 mA g^{-1}. (c) Galvanostatic charge and discharge curves of M-KTO cycled at different current densities from 20 to 300 mA g^{-1}. (d) Rate capability of M-KTO at different current densities. (e) Long-term cycling performance and Coulombic efficiency of M-KTO for PIBs at 200 mA g^{-1}.

V for M-NTO. Significantly, the subsequent cycles exhibited good reproducibility with almost overlapping of these cathodic peaks at around 0.3 and 1.0 V, demonstrating high reversibility of electrochemical reaction. Furthermore, a distinct voltage plateau between 0.3 and 0.6 V was found in the discharge profiles (Figure S9). The Coulombic efficiency of M-NTO increased promptly from 51% to 96% in the initial five cycles and thus became stable, up to 99%, in 50th cycle (Figure 5b). Importantly, M-NTO tested at 200 mA g^{-1} delivered high discharge capacities of 376, 210, and 171 mAh g^{-1} for the first, second, and 50th cycles (Figure 5b), respectively, which are higher than those of pristine Ti_3C_2 MXene (with a capacity of 263, 152, and 111 mAh g^{-1}, respectively) and commercial TiC derivative (with a capacity of 222, 97, and 64 mAh g^{-1}, respectively), clearly demonstrating enhanced sodium storage of M-NTO in terms of both high capacities and outstanding cycling stability. It is worth noting that high reversible capacity of M-NTO (192 mAh g^{-1} at 200 mA g^{-1}) outperformed most of the state-of-the-art Ti-based anodes (Table S2), for instance, $Na_2Ti_3O_7$ nanotube arrays (185 mAh g^{-1} at 177 mA g^{-1}),[47] $Na_2Ti_3O_7$/carbon (119 mAh g^{-1} at 178 mA g^{-1}),[48] $K_2Ti_6O_{13}$ nanowires (186 mAh g^{-1} at 20 mA g^{-1}),[49] and Ti_3C_2 MXene (143 mAh g^{-1} at 20 mA g^{-1}).[50] Moreover, Na-storage performance of M-NTO was also influenced by hydrothermal time and concentration of NaOH. In general, M-NTO treated with shorter (1 h) or longer (18 h) hydrothermal time (Figure S10) or in 5 M NaOH (Figure S11) exhibited low capacities and/or poor cyclability.

Remarkably, M-NTO showed extraordinary rate capability measured at varied current densities from 50 to 2000 mA g^{-1} (Figure 5c and d). With increasing current density from 50, 100, 200, 500, 1000, and 1500 to 2000 mA g^{-1}, high reversible capacities were achieved from 196 (2nd cycle), 169 (12th cycle), 153 (22th cycle), 134 (32th cycle), 119 (42th cycle), and 109 (52th cycle) to 101 mAh g^{-1} (62th cycle). Importantly, after abruptly switching the initial current density

DOI: 10.1021/acsnano.7b01165
ACS Nano 2017, 11, 4792−4800

back to 50 mA g^{-1}, a large capacity of 179 mAh g^{-1} was still restored, demonstrating the excellent robustness and stability of M-NTO. In sharp contrast, Ti_3C_2 MXene exhibited low reversible capacities of 136 (11th cycle), 125 (21th cycle), and 113 (41th cycle) at corresponding current densities of 50, 100, and 200 mA g^{-1}, respectively (Figure S12). Furthermore, long-term cyclability of M-NTO was further demonstrated for 150 cycles at 200 mA g^{-1} (Figure 5e), with an average capacity loss of 0.18% per cycle and a high Coulombic efficiency of 99.3%. Notably, the excellent electrochemical performance of M-NTO was also achieved at a higher mass loading of ~1 mg cm^{-2} (Figure S13), which was ascribed to the nanoribbon structures with suitable interlayer spacing, ultrathin thickness, and narrow widths for high utilization of active materials, enhanced ionic transport kinetics, and structural stability (Figure S14).

M-KTO was also investigated as anode for PIBs with 1.0 M KPF_6 in diglyme electrolyte (Figure 6, Figure S13). Similar to M-NTO, electrochemical reversibility of M-KTO was rapidly established in the initial three cycles, as confirmed by the overlapped second and third curves (Figure 6a). The charge−discharge reaction of $K_2Ti_4O_9$ was proposed by Brij Kishore as follows,[20] $K_2Ti_4O_9 + 2K^+ + 2e^- \leftrightarrow K_4Ti_4O_9$, in which $2Ti^{4+}$ ions in $K_2Ti_4O_9$ are reduced to $2Ti^{3+}$ ions, accompanied by insertion of 2 K^+ ions into the lattices. It is noteworthy that our M-KTO offered high initial discharge and charge capacities of 584 and 151 mAh g^{-1}, respectively, when cycled at 50 mA g^{-1}. Similar to M-NTO, high capacity was likely attributed to ultrathin nanoribbons with expanded *d*-spacing for significantly accommodating more ions in the interlayer channels. Furthermore, an interfacial potassium storage mechanism on highly active layered structures of M-KTO might contribute to the extra capacity.[51,52] After 100 cycles, a large capacity retention of 61% (the second charge capacity) with a high Coulombic efficiency of 96.6% was maintained (Figure 6b), demonstrative of outstanding cyclability. Furthermore, galvanostatic charge/discharge curves displayed pronounced K-storage behavior of M-KTO at different current densities (Figure 6c and d). The reversible capacities of 150 (1st cycle), 119 (12th cycle), 105 (22th cycle), 97 (32th cycle), 89 (42th cycle), and 81 (52th cycle) mAh g^{-1} were attained at 20, 50, 100, 150, 200, and 300 mA g^{-1}, respectively. Also, a high charge capacity of ~117 mAh g^{-1} was restored after a current density back to 20 mA g^{-1}. Importantly, the excellent rate capability (105 mAh g^{-1} at 100 mA g^{-1}, 81 mAh g^{-1} at 300 mA g^{-1}) of M-KTO nanoribbons was superior to the reported $K_2Ti_4O_9$ particles (80 mAh g^{-1} at 100 mA g^{-1})[20] and $K_2Ti_8O_{17}$ nanorods (~83 mAh g^{-1} at 100 mA g^{-1}) (Table S3).[19] Furthermore, M-KTO was validated by ultralong-term cycling life over 900 times, exhibiting a capacity retention of 51% (of the second charge capacity) and high Coulombic efficiency of 98.4% at 200 mA g^{-1} (Figure 6e) due to the robust structural integrity of ultrathin nanoribbons during cycling (Figure S15). Notably, ultrastable cyclability of M-KTO exhibited the best electrochemical performance for PIBs in the reported Ti-based nanostructures, such as potassium titanate and MXene (Table S3).[2,19,20]

CONCLUSIONS

In summary, we have demonstrated the synthesis of ultrathin M-NTO and M-KTO nanoribbons from HF-etched MXene nanosheets by a simultaneous oxidation and alkalization process under hydrothermal conditions. Benefiting from the suitable interlayer spacing, thin thickness, narrow widths, and open macroporous network, the resulting M-NTO delivered a high reversible capacity of 191 mAh g^{-1} at 200 mA g^{-1} for SIBs, and M-KTO exhibited a large reversible capacity of 151 mAh g^{-1} at 50 mA g^{-1} for PIBs, as well as outstanding rate capacity and long-term cyclability. We believe that this transformation approach is promising for developing a variety of MXene-derived nanostructured materials for numerous applications such as supercapacitors, batteries, electrocatalysts, and sensors.

METHODS

Materials Synthesis. To synthesize Ti_3C_2 MXene, typically, 1 g of Ti_3AlC_2 powder was slowly added to 120 mL of 40 wt % hydrofluoric acid solution. The reaction mixture was stirred at 300 rpm for 72 h at 25 °C. After that, the mixed solution was centrifuged at 6000 rpm for 5 min, and the powder was collected after discarding the supernatant. Then, the resulting powder was washed with distilled water repeatedly four times. Finally, Ti_3C_2 was collected by filtering the solution using a polytetrafluoroethylene membrane (0.22 mm pore size) and dried in a vacuum oven at 60 °C for 12 h.

To synthesize M-NTO and M-KTO nanoribbons, typically, 100 mg of Ti_3C_2 MXene was added into a mixed solution containing 30 mL of 1 M NaOH and 0.68 mL of 30% H_2O_2. Then, the mixed solution was transferred into a 50 mL Teflon-lined stainless-steel autoclave, which was hydrothermally treated at 140 °C for 12 h. After naturally cooling to room temperature, the upper white suspension was collected by vacuum filtration, and the resulting M-NTO sample was washed with distilled water three times and dried at 60 °C for 12 h. M-KTO was synthesized by the same procedure as M-NTO, except using KOH instead of NaOH. For comparison, 100 mg of commercial TiC particles was also hydrothermally treated with the same procedure as M-NTO, and the final product was denoted as commercial TiC derivatives.

Materials Characterizations. Materials characterizations were conducted by SEM (JEOL JSM-7800F), TEM (JEM-2100), XRD patterns (X'pert Pro), Raman (LabRam HR800 using a 633 nm laser), and XPS (Thermo Escalab 250Xi equipped with a monochromatic Al Kα source of 1486.5 eV).

Electrochemical Measurement. Both the tests of SIBs and PIBs were carried out using CR2016 coin cells with sodium or potassium foil as the counter and reference electrodes. Galvanostatic charge and discharge profiles were investigated with a LAND CT2001A battery tester. CV studies were carried out on a CHI 760E electrochemical workstation at a scan rate of 0.1 mV s^{-1}. The working electrodes (12 mm in diameter) consist of active material (Ti_3C_2 MXene, M-NTO, or M-KTO), carbon black, and polyvinylidene fluoride with a weight ratio of 7:2:1. The average mass loading on the electrodes is 0.44−1.0 mg cm^{-2}. SIB and PIB tests were conducted with 1.0 M $NaCF_3SO_3$ in diglyme electrolyte and 1.0 M KPF_6 in diglyme electrolyte between 0.01 and 3.0 V, respectively. Special attention should be paid to the danger of fabricating SIBs and PIBs due to the extremely active reactivity of alkali metals (Na, K) with water.

ASSOCIATED CONTENT

Supporting Information

The Supporting Information is available free of charge on the ACS Publications website at DOI: 10.1021/acsnano.7b01165.

Materials characterization, electrochemical characterization, and additional figures and tables (PDF)

AUTHOR INFORMATION

Corresponding Author

*E-mail (Z.-S. Wu): wuzs@dicp.ac.cn.

ORCID

Zhong-Shuai Wu: 0000-0003-1851-4803

Xiaohui Wang: 0000-0001-7271-2662

DOI: 10.1021/acsnano.7b01165
ACS Nano 2017, 11, 4792−4800

Xinhe Bao: 0000-0001-9404-6429

Author Contributions

Z.S.W. and X.H.B. proposed and supervised the overall project. Y.F.D. did the fabrication and electrochemical measurement of M-NTO and M-KTO. Y.F.D. and Z.S.W. analyzed the data. X.H.W. prepared the MAX phase. S.H.Z., J.Q.Q., S.W., and X.Y.S. participated in the structural characterization of the related materials. Y.F.D., Z.S.W., and X.H.B. cowrote the paper. All authors commented and have given approval to the final version of the manuscript.

Notes

The authors declare no competing financial interest.

ACKNOWLEDGMENTS

This work was financially supported by the National Key R&D Program of China (Grants 2016YBF0100100 and 2016YFA0200200), National Natural Science Foundation of China (Grant 51572259), Natural Science Foundation of Liaoning Province (Grant 201602737), Thousand Youth Talents Plan of China, DICP (Grant Y5610121T3), China Postdoctoral Science Foundation (Grant 2016M601349), and dedicated funds for methanol conversion from DICP.

REFERENCES

(1) Goodenough, J. B.; Park, K.-S. The Li-Ion Rechargeable Battery: A Perspective. *J. Am. Chem. Soc.* **2013**, *135*, 1167−1176.
(2) Xie, Y.; Dall'Agnese, Y.; Naguib, M.; Gogotsi, Y.; Barsoum, M. W.; Zhuang, H. L.; Kent, P. R. C. Prediction and Characterization of MXene Nanosheet Anodes for Non-Lithium-Ion Batteries. *ACS Nano* **2014**, *8*, 9606−9615.
(3) Kundu, D.; Talaie, E.; Duffort, V.; Nazar, L. F. The Emerging Chemistry of Sodium Ion Batteries for Electrochemical Energy Storage. *Angew. Chem., Int. Ed.* **2015**, *54*, 3431−3448.
(4) Mei, Y.; Huang, Y.; Hu, X. Nanostructured Ti-Based Anode Materials for Na-Ion Batteries. *J. Mater. Chem. A* **2016**, *4*, 12001−12013.
(5) Yabuuchi, N.; Kubota, K.; Dahbi, M.; Komaba, S. Research Development on Sodium-Ion Batteries. *Chem. Rev.* **2014**, *114*, 11636−11682.
(6) Eftekhari, A.; Jian, Z.; Ji, X. Potassium Secondary Batteries. *ACS Appl. Mater. Interfaces* **2017**, *9*, 4404−4419.
(7) Slater, M. D.; Kim, D.; Lee, E.; Johnson, C. S. Sodium-Ion Batteries. *Adv. Funct. Mater.* **2013**, *23*, 947−958.
(8) Zhao, J.; Zou, X.; Zhu, Y.; Xu, Y.; Wang, C. Electrochemical Intercalation of Potassium into Graphite. *Adv. Funct. Mater.* **2016**, *26*, 8103−8110.
(9) Luo, W.; Wan, J.; Ozdemir, B.; Bao, W.; Chen, Y.; Dai, J.; Lin, H.; Xu, Y.; Gu, F.; Barone, V.; Hu, L. Potassium Ion Batteries with Graphitic Materials. *Nano Lett.* **2015**, *15*, 7671−7677.
(10) Jian, Z.; Xing, Z.; Bommier, C.; Li, Z.; Ji, X. Hard Carbon Microspheres: Potassium-Ion Anode *Versus* Sodium-Ion Anode. *Adv. Energy Mater.* **2016**, *6*, 1501874.
(11) Liu, Y.; Fan, F.; Wang, J.; Liu, Y.; Chen, H.; Jungjohann, K. L.; Xu, Y.; Zhu, Y.; Bigio, D.; Zhu, T.; Wang, C. *In Situ* Transmission Electron Microscopy Study of Electrochemical Sodiation and Potassiation of Carbon Nanofibers. *Nano Lett.* **2014**, *14*, 3445−3452.
(12) Kim, H.; Hong, J.; Park, Y.-U.; Kim, J.; Hwang, I.; Kang, K. Sodium Storage Behavior in Natural Graphite Using Ether-Based Electrolyte Systems. *Adv. Funct. Mater.* **2015**, *25*, 534−541.
(13) Jian, Z.; Luo, W.; Ji, X. Carbon Electrodes for K-Ion Batteries. *J. Am. Chem. Soc.* **2015**, *137*, 11566−11569.
(14) Li, H.; Peng, L.; Zhu, Y.; Chen, D.; Zhang, X.; Yu, G. An Advanced High-Energy Sodium Ion Full Battery Based on Nanostructured $Na_2Ti_3O_7$/$VOPO_4$ Layered Materials. *Energy Environ. Sci.* **2016**, *9*, 3399−3405.
(15) Pan, H.; Lu, X.; Yu, X.; Hu, Y.-S.; Li, H.; Yang, X.-Q.; Chen, L. Sodium Storage and Transport Properties in Layered $Na_2Ti_3O_7$ for Room-Temperature Sodium-Ion Batteries. *Adv. Energy Mater.* **2013**, *3*, 1186−1194.
(16) Wu, D.; Li, X.; Xu, B.; Twu, N.; Liu, L.; Ceder, G. $NaTiO_2$: A Layered Anode Material for Sodium-Ion Batteries. *Energy Environ. Sci.* **2015**, *8*, 195−202.
(17) Fu, S.; Ni, J.; Xu, Y.; Zhang, Q.; Li, L. Hydrogenation Driven Conductive $Na_2Ti_3O_7$ Nanoarrays as Robust Binder-Free Anodes for Sodium-Ion Batteries. *Nano Lett.* **2016**, *16*, 4544−4551.
(18) Wang, W.; Yu, C.; Lin, Z.; Hou, J.; Zhu, H.; Jiao, S. Microspheric $Na_2Ti_3O_7$ Consisting of Tiny Nanotubes: An Anode Material for Sodium-Ion Batteries with Ultrafast Charge-Discharge Rates. *Nanoscale* **2013**, *5*, 594−599.
(19) Han, J.; Xu, M.; Niu, Y.; Li, G.-N.; Wang, M.; Zhang, Y.; Jia, M.; Li, C. M. Exploration of $K_2Ti_8O_{17}$ as An Anode Material for Potassium-Ion Batteries. *Chem. Commun.* **2016**, *52*, 11274−11276.
(20) Kishore, B.; G, V.; Munichandraiah, N. $K_2Ti_4O_9$: A Promising Anode Material for Potassium Ion Batteries. *J. Electrochem. Soc.* **2016**, *163*, A2551−A2554.
(21) Ling, Z.; Ren, C. E.; Zhao, M.-Q.; Yang, J.; Giammarco, J. M.; Qiu, J.; Barsoum, M. W.; Gogotsi, Y. Flexible and Conductive MXene Films and Nanocomposites with High Capacitance. *Proc. Natl. Acad. Sci. U. S. A.* **2014**, *111*, 16676−16681.
(22) Ghidiu, M.; Lukatskaya, M. R.; Zhao, M.-Q.; Gogotsi, Y.; Barsoum, M. W. Conductive Two-Dimensional Titanium Carbide 'Clay' with High Volumetric Capacitance. *Nature* **2014**, *516*, 78−81.
(23) Li, H.; Hou, Y.; Wang, F.; Lohe, M. R.; Zhuang, X.; Niu, L.; Feng, X. Flexible All-Solid-State Supercapacitors with High Volumetric Capacitances Boosted by Solution Processable MXene and Electrochemically Exfoliated Graphene. *Adv. Energy Mater.* **2017**, *7*, 1601847.
(24) Tang, Q.; Zhou, Z. Graphene-Analogous Low-Dimensional Materials. *Prog. Mater. Sci.* **2013**, *58*, 1244−1315.
(25) Luo, J.; Tao, X.; Zhang, J.; Xia, Y.; Huang, H.; Zhang, L.; Gan, Y.; Liang, C.; Zhang, W. Sn^{4+} Ion Decorated Highly Conductive Ti_3C_2 MXene: Promising Lithium-Ion Anodes with Enhanced Volumetric Capacity and Cyclic Performance. *ACS Nano* **2016**, *10*, 2491−2499.
(26) Lukatskaya, M. R.; Mashtalir, O.; Ren, C. E.; Dall'Agnese, Y.; Rozier, P.; Taberna, P. L.; Naguib, M.; Simon, P.; Barsoum, M. W.; Gogotsi, Y. Cation Intercalation and High Volumetric Capacitance of Two-Dimensional Titanium Carbide. *Science* **2013**, *341*, 1502−1505.
(27) Shahzad, F.; Alhabeb, M.; Hatter, C. B.; Anasori, B.; Man Hong, S.; Koo, C. M.; Gogotsi, Y. Electromagnetic Interference Shielding with 2D Transition Metal Carbides (MXenes). *Science* **2016**, *353*, 1137−1140.
(28) Hope, M. A.; Forse, A. C.; Griffith, K. J.; Lukatskaya, M. R.; Ghidiu, M.; Gogotsi, Y.; Grey, C. P. NMR Reveals the Surface Functionalisation of Ti_3C_2 MXene. *Phys. Chem. Chem. Phys.* **2016**, *18*, 5099−5102.
(29) Halim, J.; Cook, K. M.; Naguib, M.; Eklund, P.; Gogotsi, Y.; Rosen, J.; Barsoum, M. W. X-Ray Photoelectron Spectroscopy of Select Multi-Layered Transition Metal Carbides (MXenes). *Appl. Surf. Sci.* **2016**, *362*, 406−417.
(30) Er, D.; Li, J.; Naguib, M.; Gogotsi, Y.; Shenoy, V. B. Ti_3C_2 MXene as A High Capacity Electrode Material for Metal (Li, Na, K, Ca) Ion Batteries. *ACS Appl. Mater. Interfaces* **2014**, *6*, 11173−11179.
(31) Lei, J.-C.; Zhang, X.; Zhou, Z. Recent Advances in MXene: Preparation, Properties, and Applications. *Front. Phys.* **2015**, *10*, 276−286.
(32) Tang, Q.; Zhou, Z.; Shen, P. Are MXenes Promising Anode Materials for Li Ion Batteries? Computational Studies on Electronic Properties and Li Storage Capability of Ti_3C_2 and $Ti_3C_2X_2$ (X = F, OH) Monolayer. *J. Am. Chem. Soc.* **2012**, *134*, 16909−16916.
(33) Zhang, C.; Kim, S. J.; Ghidiu, M.; Zhao, M.-Q.; Barsoum, M. W.; Nicolosi, V.; Gogotsi, Y. Layered Orthorhombic Nb_2O_5@$Nb_4C_3T_x$ and TiO_2@Ti_3C_2Tx Hierarchical Composites for High Performance Li-Ion Batteries. *Adv. Funct. Mater.* **2016**, *26*, 4143−4151.
(34) Hu, M.; Li, Z.; Hu, T.; Zhu, S.; Zhang, C.; Wang, X. High-Capacitance Mechanism for $Ti_3C_2T_x$ MXene by *In Situ* Electro-

DOI: 10.1021/acsnano.7b01165
ACS Nano 2017, 11, 4792−4800

chemical Raman Spectroscopy Investigation. *ACS Nano* **2016**, *10*, 11344−11350.
(35) Naguib, M.; Kurtoglu, M.; Presser, V.; Lu, J.; Niu, J. J.; Heon, M.; Hultman, L.; Gogotsi, Y.; Barsoum, M. W. Two-Dimensional Nanocrystals Produced by Exfoliation of Ti_3AlC_2. *Adv. Mater.* **2011**, *23*, 4248−4253.
(36) Naguib, M.; Mashtalir, O.; Carle, J.; Presser, V.; Lu, J.; Hultman, L.; Gogotsi, Y.; Barsoum, M. W. Two-Dimensional Transition Metal Carbides. *ACS Nano* **2012**, *6*, 1322−1331.
(37) Kurra, N.; Ahmed, B.; Gogotsi, Y.; Alshareef, H. N. MXene-on-Paper Coplanar Microsupercapacitors. *Adv. Energy Mater.* **2016**, *6*, 1601372.
(38) Naguib, M.; Mochalin, V. N.; Barsoum, M. W.; Gogotsi, Y. 25th Anniversary Article: MXenes: A New Family of Two-Dimensional Materials. *Adv. Mater.* **2014**, *26*, 992−1005.
(39) Feng, M.; You, W.; Wu, Z.; Chen, Q.; Zhan, H. Mildly Alkaline Preparation and Methylene Blue Adsorption Capacity of Hierarchical Flower-Like Sodium Titanate. *ACS Appl. Mater. Interfaces* **2013**, *5*, 12654−12662.
(40) Zhang, Z.; Goodall, J. B.; Brown, S.; Karlsson, L.; Clark, R. J.; Hutchison, J. L.; Rehman, I. U.; Darr, J. A. Continuous Hydrothermal Synthesis of Extensive 2D Sodium Titanate ($Na_2Ti_3O_7$) Nanosheets. *Dalton Trans.* **2010**, *39*, 711−714.
(41) Dong, S.; Shen, L.; Li, H.; Pang, G.; Dou, H.; Zhang, X. Flexible Sodium-Ion Pseudocapacitors Based on 3D $Na_2Ti_3O_7$ Nanosheet Arrays/Carbon Textiles Anodes. *Adv. Funct. Mater.* **2016**, *26*, 3703−3710.
(42) Kasuga, T.; Hiramatsu, M.; Hoson, A.; Sekino, T.; Niihara, K. Titania Nanotubes Prepared by Chemical Processing. *Adv. Mater.* **1999**, *11*, 1307−1311.
(43) Ahmed, B.; Anjum, D. H.; Hedhili, M. N.; Gogotsi, Y.; Alshareef, H. N. H_2O_2 Assisted Room Temperature Oxidation of Ti_2C MXene for Li-Ion Battery Anodes. *Nanoscale* **2016**, *8*, 7580−7587.
(44) Tang, Y.; Zhang, Y.; Deng, J.; Wei, J.; Le Tam, H.; Chandran, B. K.; Dong, Z.; Chen, Z.; Chen, X. Mechanical Force-Driven Growth of Elongated Bending TiO_2-Based Nanotubular Materials for Ultrafast Rechargeable Lithium Ion Batteries. *Adv. Mater.* **2014**, *26*, 6111−6118.
(45) Dong, Y.; Yu, M.; Wang, Z.; Liu, Y.; Wang, X.; Zhao, Z.; Qiu, J. A Top-Down Strategy toward 3D Carbon Nanosheet Frameworks Decorated with Hollow Nanostructures for Superior Lithium Storage. *Adv. Funct. Mater.* **2016**, *26*, 7590−7598.
(46) Li, N.; Chen, Z.; Ren, W.; Li, F.; Cheng, H.-M. Flexible Graphene-Based Lithium Ion Batteries with Ultrafast Charge and Discharge Rates. *Proc. Natl. Acad. Sci. U. S. A.* **2012**, *109*, 17360−17365.
(47) Ni, J.; Fu, S.; Wu, C.; Zhao, Y.; Maier, J.; Yu, Y.; Li, L. Superior Sodium Storage in $Na_2Ti_3O_7$ Nanotube Arrays through Surface Engineering. *Adv. Energy Mater.* **2016**, *6*, 1502568.
(48) Yan, Z.; Liu, L.; Shu, H.; Yang, X.; Wang, H.; Tan, J.; Zhou, Q.; Huang, Z.; Wang, X. A Tightly Integrated Sodium Titanate-Carbon Composite as An Anode Material for Rechargeable Sodium Ion Batteries. *J. Power Sources* **2015**, *274*, 8−14.
(49) Zhang, Q.; Guo, Y.; Guo, K.; Zhai, T.; Li, H. Ultrafine Potassium Titanate Nanowires: A New Ti-Based Anode for Sodium Ion Batteries. *Chem. Commun.* **2016**, *52*, 6229−6232.
(50) Kajiyama, S.; Szabova, L.; Sodeyama, K.; Iinuma, H.; Morita, R.; Gotoh, K.; Tateyama, Y.; Okubo, M.; Yamada, A. Sodium-Ion Intercalation Mechanism in MXene Nanosheets. *ACS Nano* **2016**, *10*, 3334−3341.
(51) Wang, J.; Yang, N.; Tang, H.; Dong, Z.; Jin, Q.; Yang, M.; Kisailus, D.; Zhao, H.; Tang, Z.; Wang, D. Accurate Control of Multishelled Co_3O_4 Hollow Microspheres as High-Performance Anode Materials in Lithium-Ion Batteries. *Angew. Chem., Int. Ed.* **2013**, *52*, 6417−6420.
(52) Maier, J. Nanoionics: Ion Transport and Electrochemical Storage in Confined Systems. *Nat. Mater.* **2005**, *4*, 805−815.

DOI: 10.1021/acsnano.7b01165
ACS Nano 2017, 11, 4792−4800